



OPEN Investigating the scale effect on strength and failure mechanism of roadway surrounding rock

Jingke Wu¹, Fuxing Xie²✉ & Yunfei Wang³

An analysis model for surrounding rock was established, considering excavation-induced damage and failure zones. Meso-mechanical parameters for Particle Flow Code (PFC) were calibrated using sandstone test data from Brazilian splitting, uniaxial, and triaxial tests. The strength variation of multi-scale surrounding rock was investigated: at a fixed width of 50 mm, the strength decreases linearly as height increases from 20 to 80 mm, then increases with height from 80 to 300 mm; at a fixed height of 100 mm, the strength increases linearly with width from 20 to 300 mm. The ratio of damage stress to strength (multi-scale surrounding rock with a width of 50 mm)/the second ratio of damage stress to strength (with a height of 100 mm) does not change with height/width, which is approximately 0.91. The mechanical mechanism of only shallow failure or zonal disintegration characteristics of the surrounding rock were revealed by analyzing the failure characteristics of multi-scale surrounding rock: under shallow burial conditions, a narrow stress concentration zone leads to only shallow failure, whereas under deep burial, a wider stress concentration zone leads to both shallow failure and zonal disintegration. These findings provide a theoretical basis for stability assessment of underground roadway surrounding rock.

Keywords Multi-scale, Surrounding rock, Strength, Failure characteristics, Mechanical mechanism

The stability analysis of various rock mass engineering requires consideration of the strength and deformation parameters of the rock mass. The mechanical properties of the rock mass are also related to its scale characteristics. This has been a long-standing challenge in rock mechanics, unresolved for over 70 years since its proposal at the Geomechanics Symposium in 1950¹.

Rock mechanics researchers have conducted extensive studies on the strength and failure modes of rocks at different scales. Sun et al. conducted multi-scale analysis on roadway surrounding rock and concluded that macroscopic fracture of deep surrounding rock is mainly controlled by localized regional fragmentation. As the scale increases, the failure of the surrounding rock exhibits shear sliding and plate splitting². Darlington et al. emphasized the close link between scale effect and rock type through statistical analysis of existing experimental data³. Zaytsev et al. found that the average tensile strength of granite decreases with increasing sample size⁴, while Asadi⁵ and Li et al.⁶ explored the combined impacts of loading rate and sample size on rock tensile strength, noting that the scale effect on tensile strength is minimized under a critical stress rate and establishing a scale effect equation. Lei et al. divided scale effect into volume effect and aspect ratio effect and analyzed their respective influences on compressive strength⁷. Kashfi et al.⁸ identified an aspect ratio of 3 as the optimal proportion for the stress–strain uniformity index via multi-scale finite element analysis, and Chen et al.⁹ discovered a strength turning point when the aspect ratio reaches 2. Qian et al.¹⁰ and Wen et al.¹¹ studied the strength degradation of rock and the failure characteristics of rock under dynamic and static stress. For jointed rock masses, Azinfar et al.¹² examined the scale effect on shear strength, Dong et al.¹³ found that strength decreases with increasing scale at the same joint dip angle, and Ma et al.¹⁴ indicated through numerical simulations that jointed rock mass strength stabilizes at a scale of 4 m × 4 m × 8 m. Additionally, Zhang et al.¹⁵, Wang et al.¹⁶, and Bewick et al.¹⁷ utilized particle flow code to study the size effect on intact/jointed rock mass strength and crack propagation, Liu et al.¹⁸ revealed that rock strength decreases with height and increases with width via discrete element analysis, and Li et al.¹⁹ explored the relationship between static and dynamic compressive strength using cubic and cylindrical concrete samples. Overall, these studies elucidate how scale, rock type and joint characteristics affect the strength and failure behavior of rocks or rock masses.

¹School of Intelligent Manufacturing and Smart Transportation, Suzhou City University, Suzhou 215104, China.

²Beijing China Coal Mine Engineering Co., Ltd., Beijing 100013, China. ³School of Civil Engineering, Henan Polytechnic University, Jiaozuo 454003, Henan, China. ✉email: fxxcumt@126.com

In establishing strength criteria and predictive models to quantify rock or surrounding rock strength, Brook²⁰ developed a strength method for equivalent circular cross-section samples through tests on non-circular cross-section samples, and Rajmeny et al.²¹ constructed strength models for surrounding rock with different opening sizes. Pankov²² proposed a tensile and biaxial compressive strength criterion considering three principal stresses, Masoumi et al.²³ put forward a multiaxial strength criterion incorporating a scale effect parameter, and Mehranpour et al.²⁴ built a three-dimensional strength criterion to analyze the coupling effects of rock mass anisotropy and scale effect. Mahmoodzadeh et al.²⁵ employed four machine learning techniques to develop a strength prediction model, which estimates internal friction angle and cohesion using uniaxial compressive strength, tensile strength, and confining pressure as input parameters. These works provide theoretical frameworks for predicting and evaluating the strength of rocks and surrounding rocks in engineering applications.

Based on the comprehensive analysis of the existing research results, it can be concluded that the strength and failure characteristics mainly focus on the scale effect under the uniaxial stress path of the rock, as well as the strength model that comprehensively considers the influence of the joint and confining pressure. However, both uniaxial and triaxial conditions do not match the actual stress conditions of the surrounding rock of roadway. Therefore, this research constructed a surrounding rock analysis model of roadway considering the characteristics of the damaged and fractured areas of the surrounding rock (Fig. 6), and studies the strength and failure characteristics of multi scale surrounding rock.

Sandstone test data and meso-parameters PFC model selection

The PFC discrete element can directly simulate rock damage and macroscopic mechanical behavior by selecting appropriate particle contact model and assigning mesoscopic parameters (Fig. 1a,b), without the need to consider complex constitutive relationships²⁶. Notably, Potyondy proposed a flat-joint model that effectively captures the high compressive-to-tensile strength ratio characteristic of rock, which has since become widely adopted for rock simulations^{27,28}. Accordingly, this model is employed in the present study.

The flat-joint model is composed of piece and contact (Fig. 1c–d), and a piece is composed of circular particle and notional surfaces (Fig. 1d). A piece may have multiple ideal notional surfaces; hence, the flat-joint model constructs circular particles into polygons (Fig. 1c), which has a sufficient self-locking effect, inhibits the rotation of particles, and may be used in the analysis of rock materials. In PFC2D, the contact interface is a straight line segment and can be divided into multiple elements (Fig. 1c). Each element on the contact interface can be bonded or frictional. Therefore, the contacts in the flat-joint model may undergo deformation, failure, or localized damage (Fig. 1c). After a bond failure, it changes into a slip model (Fig. 2), as described by Eqs. (1) and (2).

$$\tau_s = c + \sigma \tan \varphi, \quad (1)$$

$$\tau_s = \mu\sigma, \quad (2)$$

where τ_s is the bond or slip shear strength, c is the cohesion, φ is the internal friction angle, μ is the friction coefficient, σ is the compressive stress acting on the element, and σ_t is the bond tensile strength.

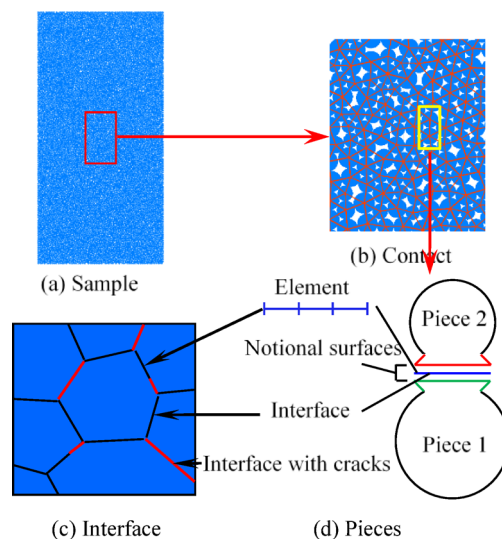


Fig. 1. Flat-joint contact and material.

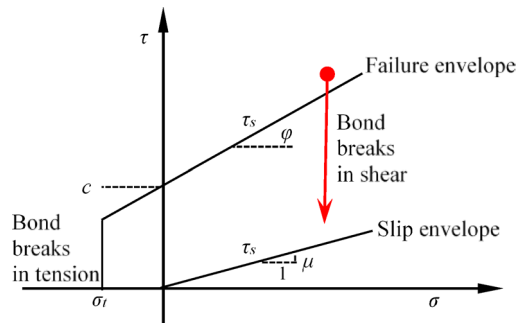


Fig. 2. Failure and slip envelopes for a bonded or unbonded flat-joint element.

E^* (GPa)	k^*	σ^* (MPa)	c (MPa)	φ (°)	μ
15	4.8	9.0	49	8.0	0.35

Table 1. Meso-parameters of the flat-joint model.

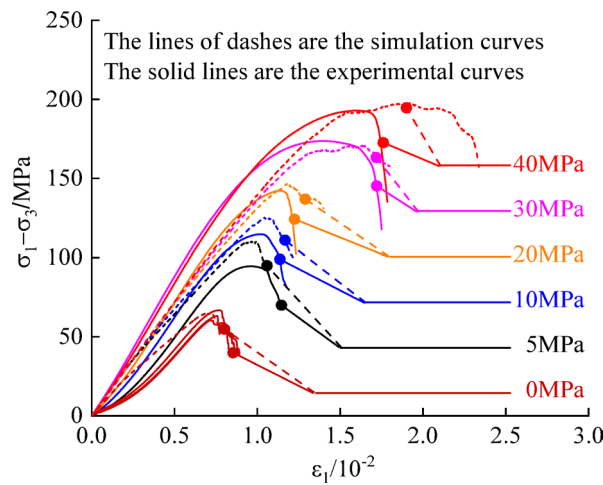


Fig. 3. Comparison of stress–strain curves between experimental and numerical simulation.

Sandstone mechanical and meso-parameters

The meso-parameters, including the tensile strength (σ^*), cohesion (c), friction coefficient (μ), friction angle (φ), effective modulus (E^*) and normal-to-shear stiffness ratio (k^*), were determined based on sandstone experimental data²⁹, as listed in Table 1.

The meso-parameters listed in Table 1 were employed to simulate sandstone behavior. A comparative analysis was conducted between the experimental results²⁹ and numerical simulations in terms of stress–strain curves (Fig. 3), strength envelopes (Fig. 4), and failure patterns (Fig. 5).

In Fig. 3, although some discrepancies exist between the simulated and experimental curves, the numerical model demonstrates good agreement with the experimental data in terms of sandstone strength, peak strain, and overall deformation trends. Figure 4 illustrates that the strength envelope of sandstone is well fitted as a whole. The tensile strength is not shown in Fig. 4. The experimental and simulated tensile strength are 2.92 and 2.98 MPa, respectively, which are very close. Figure 5 shows that the failure characteristics of the PFC samples under Brazilian splitting, uniaxial, and triaxial compression tests are very close to those of the sandstone samples.

According to the comprehensive analysis of the stress–strain curves, strength envelope, and failure characteristics, the PFC model and its meso-parameters selected in this section can well reflect the macro mechanical properties of sandstone and provide reliable parameters for the analysis of multi-scale surrounding rock in “Scale effect of strength and deformation of the roadway surrounding rock” Section.

Scale effect of strength and deformation of the roadway surrounding rock Constructing the analysis model of roadway surrounding rock

The excavation of underground engineering disturbs the in situ stress balance, the stress is constantly adjusted, and the stress concentration occurs around the roadway. When the stress reaches or exceeds the strength of the

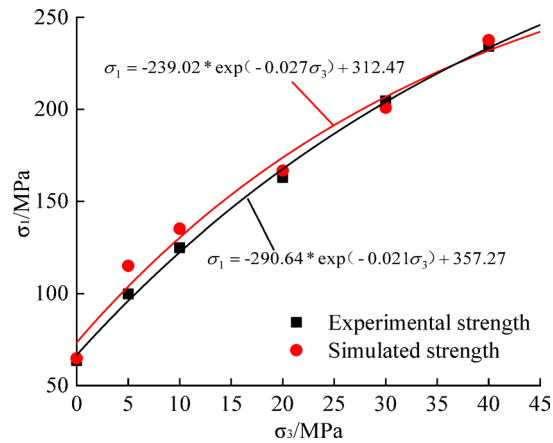


Fig. 4. Comparison of strength envelope between experimental and numerical simulation.

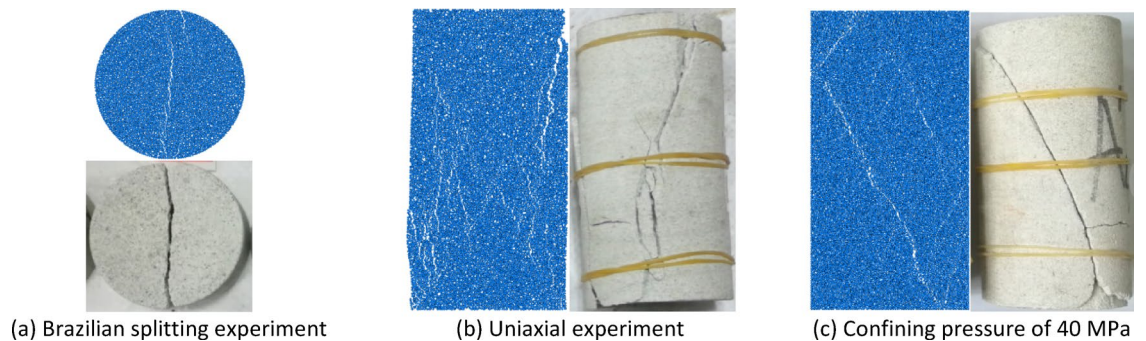


Fig. 5. Comparison of the sample failure characteristics between experimental and numerical simulation.

rock mass, the rock mass fails, and the cracks extend to the deep rock mass until the stress balance is reached again. Figure 6a,b show the failure diagram of the surrounding rock and support of iron mine roadway. The surrounding rock is divided into three zones, namely, failure, damage, and intact zones, according to the failure characteristics of the surrounding rock of the roadway, and their 3D and plane models are shown in Fig. 6c. The discrete element analysis model of PFC was constructed by analyzing Fig. 6a,b in combination with Fig. 6c, and Fig. 6d. The numerical model is constructed according to the three zones of the surrounding rock, as shown in Fig. 6d. The loading is carried out in the failure zone to simulate the failure characteristics of the surrounding rock adjacent to the roadway. The damage zone simulates the microcrack development zone caused by the development of failure zone. The intact zone represents the internal rock mass that is basically not affected by excavation.

Figure 6d is the analysis model of the surrounding rock strength and failure characteristics. The right side of the model is the free surface formed by roadway excavation, and the left side is the same rock mass that can be cooperatively deformed. In the uniaxial compressive test of rock, both sides are free surfaces. In the triaxial compressive tests, both sides have fixed confining pressure. The analysis model constructed in this work is more in line with the actual stress case of the surrounding rock of underground engineering compared with uniaxial and triaxial tests, indicating that the model is more scientific and reasonable.

The strength and failure characteristics of the multi-scale surrounding rock were analyzed by using the surrounding rock analysis model in Fig. 6 and the meso-parameters obtained in Section "Sandstone test data and meso-parameters". Two research schemes were adopted. Scheme 1: the width of the failure zone of the sample is 50 mm, and the heights are 20, 30, 40, 50, 60, 70, 80, 90, 100, 120, 140, 160, 180, 200, 220, 240, 260, 280, and 300 mm. Scheme 2: the height of the failure zone of the sample is 100 mm, and the widths are 20, 30, 40, 50, 60, 70, 80, 90, 100, 120, 140, 160, 180, 200, 220, 240, 260, 280, and 300 mm.

Scale effect of strength of the surrounding rock

Figure 7 illustrates the location and zone of data acquisition for analyzing stain and damage stress. ①, ②, ③, ④, and ⑤ in Fig. 7 are deformation monitoring lines, and 13 data monitoring points are set at equal intervals along each line. The top, middle, and bottom zones are three zones for analyzing the volume strain in Section "Scale effect of the deformation characteristics".

The stress-strain curves of the failure process of the roadway surrounding rock in schemes 1 and 2 are plotted in Fig. 8.

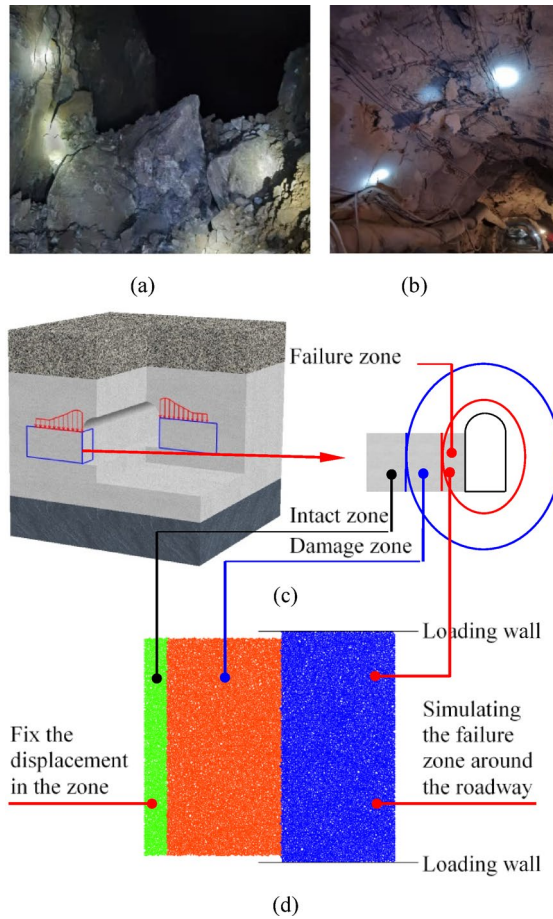


Fig. 6. Construction of the analysis model of the surrounding rock.

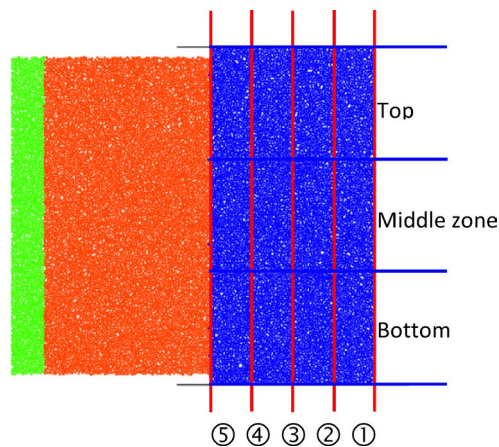
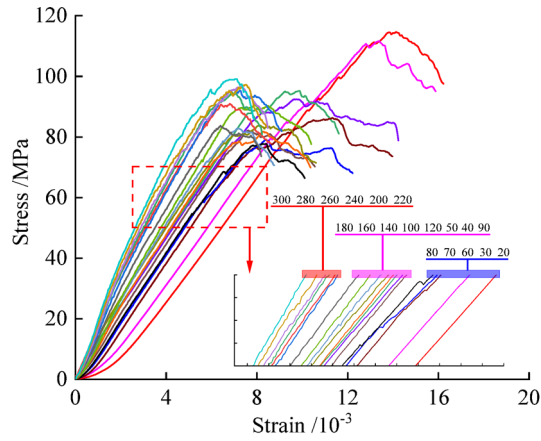


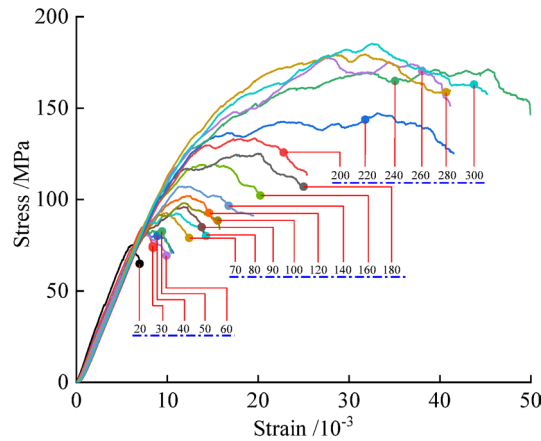
Fig. 7. Deformation data acquisition lines and zones for analyzing volume strain.

Figure 8a shows that the elastic modulus of the multi-scale surrounding rock with a failure zone width of 50 mm increases, and the peak strain decreases as a whole when the height of sample increases from 20 to 300 mm. The yield characteristics are obvious when the height is 50–180 mm, that is, the yield characteristics are obvious when the height to width ratio is 1.0–3.6.

Figure 8b shows that the elastic modulus of the multi-scale surrounding rock with a failure zone height of 100 mm basically does not change with the increase in width. The peak strain increases as a whole with the increase in width. When the width is greater than 70 mm, the yield characteristic is obvious, that is, when the width to

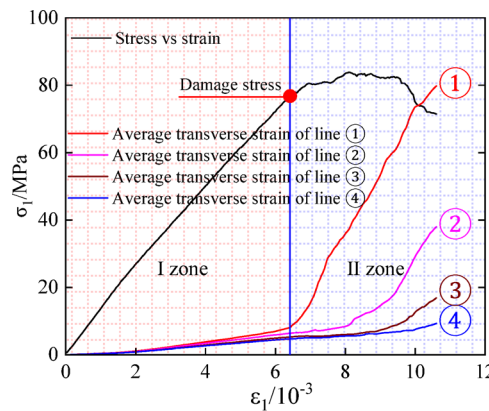


(a) The width is 50 mm

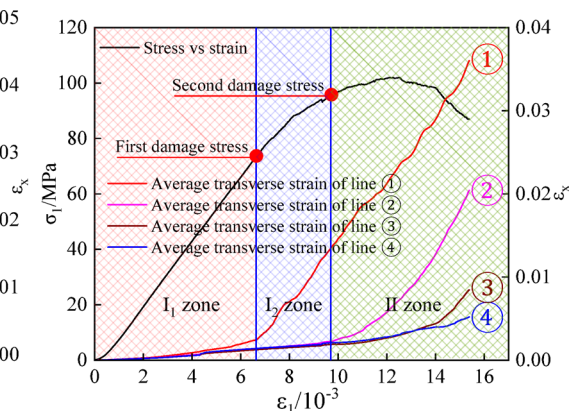


(b) The height is 100 mm

Fig. 8. Stress–strain curves of the multi-scale surrounding rock.



(a) Damage stress



(b) First/Second damage stress

Fig. 9. Determination of damage stress.

height ratio is greater than 0.7, the yield characteristics is obvious, and the yield stage significantly increases with the increase in width.

Based on the data obtained from ① to ⑤ deformation monitoring lines in Fig. 7, the average transverse strain at each monitoring line was calculated, and the damage stress was determined according to the variation characteristics of the transverse strain at different monitoring lines, as shown in Fig. 9. In Fig. 9, ① line transverse strain = increment of transverse distance between ① line and ③ line/initial transverse distance between ① line

and ⑤ line, and the calculation of ②–④ line transvers strain is similar. The stress determined by ϵ_1 corresponding to the obvious nonlinear increase of the transverse strain is defined as damage stress, as shown in Fig. 9a. Taking the damage stress as the boundary, the rock failure process is divided into I zone and II zone. I zone corresponds to the elastic deformation and microcrack formation stage, and II zone corresponds to the rapid development of microcracks until the rock fails. In Fig. 9b, the stress corresponding to the rapid increase of ① line transverse strain is defined as the first damage stress. Meanwhile, the stress corresponding to the rapid increase of ②–④ line transverse strains is defined as second damage stress. Taking the first and second damage stresses as the boundary, the rock failure process is divided into I_1 , I_2 , and II zones. I_1 zone corresponds to the elastic deformation and microcrack formation stage of the shallow surrounding rock, I_2 zone corresponds to the elastic deformation and microcrack formation stage of the deep surrounding rock and the rapid development of cracks of the shallow surrounding rock. II zone corresponds to the overall rapid development of the surrounding rock cracks until the surrounding rock fails.

Only one damage stress occurs in the surrounding rock with width of 50 mm and height change, which is called damage stress, during the failure process of multi-scale surrounding rock, as shown in Fig. 9(a). In the surrounding rock with a height of 100 mm and width change, there are two obvious damage stresses when the width is greater than 70 mm, which are called as first and second damage stresses, as shown in Fig. 9b. The first damage stress corresponds to the microcrack rapid development of the shallow surrounding rock. The second damage stress corresponds to the microcrack rapid development of the deep surrounding rock.

Figure 10a illustrates that when the width of the surrounding rock failure zone is 50 mm, the strength of the multi-scale surrounding rock first decreases and then increases with the increase of height. When the height is 20 mm, the strength is the maximum. When the height is 80 mm, the strength is the minimum, and when the height increases from 80 to 300 mm. The strength begins to linearly increases again. The variation gradient of strength in the height range of 20–80 mm is greater than that in the height range of 80–300 mm. The linear law of the change of the multi-scale surrounding rock strength with the increase in height can be expressed by Eqs. (3)–(4). The change law of damage stress of the surrounding rock with a width of 50 mm in the failure zone is similar to that of the strength with the increase in height and presents a linear law of first decreasing and then increasing, as shown in Eqs. (5)–(6).

$$\sigma_1 = 123.55 - 0.5728H \quad (20 \leq H \leq 80) \tag{3}$$

$$\sigma_1 = 69.42 + 0.1041H \quad (80 < H \leq 300) \tag{4}$$

$$\sigma_{DS} = 103.01 - 0.3739H \quad (20 \leq H \leq 80) \tag{5}$$

$$\sigma_{DS} = 65.94 + 0.0898H \quad (80 < H \leq 300) \tag{6}$$

Figure 10b illustrates that when the height of the surrounding rock failure zone is 100 mm, the strength of the multi-scale surrounding rock linearly increases with the increase in width. The variation law is shown in Eq. (7). According to the definition in Fig. 9b, the first and second damage stresses obtained are plotted in Fig. 10(b). The variation laws of the first and second damage stresses with the increase in width are shown in Eqs. (8) and (9), respectively.

$$\sigma_1 = 67.51 + 0.3754W \quad (20 \leq W \leq 300) \tag{7}$$

$$\sigma_{FDS} = 72.07 + 0.0746W \quad (20 \leq W \leq 300) \tag{8}$$

$$\sigma_{SDS} = 67.83 + 0.2837W \quad (70 \leq W \leq 300) \tag{9}$$

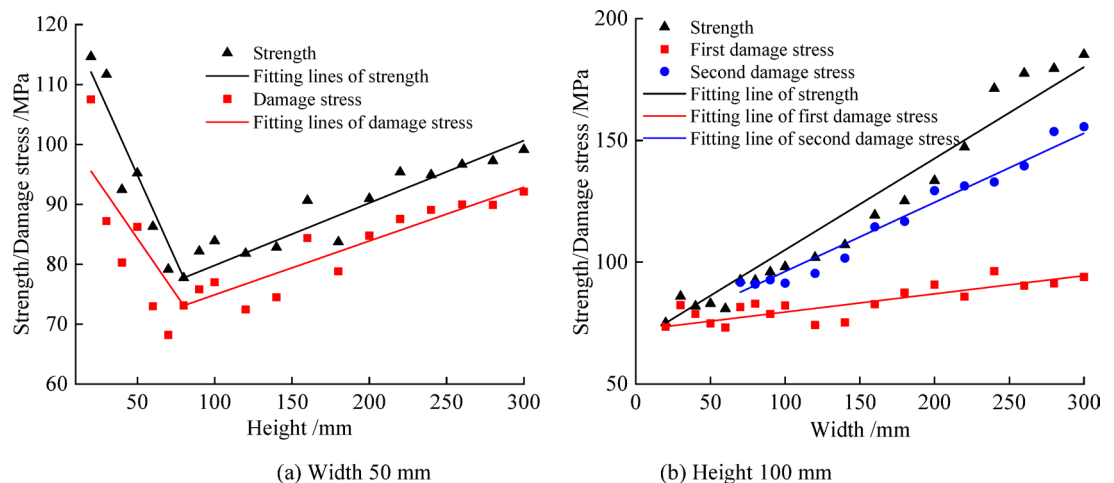


Fig. 10. Variation of strength of the multi-scale surrounding rock with width/height.

Figure 11 illustrates that the width of the failure zone of the surrounding rock is 50 mm. The damage stress to strength ratio of the surrounding rock changes less with the increase in height, with an average value of 0.91. When the height of the failure zone of the surrounding rock is 100 mm, the first damage stress to strength ratio of the surrounding rock significantly decreases with the increase in width. The second damage stress to strength ratio changes less with the increase in width, and the average value is also 0.91.

Scale effect of the deformation characteristics

To analyze the volume strain distribution characteristics of the multi-scale surrounding rock at peak stress, the volume strain was calculated according to $\varepsilon_V = \varepsilon_x + \varepsilon_y$, where, ε_V , ε_x , and ε_y represent the volume strain, transverse, and longitudinal strain, respectively. The distributions of volume strain are shown in Figs. 12 and 13. In Fig. 7, the failure zone of the surrounding rock is divided into top, middle, and bottom zones, and the volume strain variation law of the different zones is further analyzed, as shown in Fig. 14.

The number 5050 in Fig. 12a indicates that the width of the failure zone of the surrounding rock is 50 mm, and the height is 50 mm. The other numbers in Figs. 12 and 13 are similar. Figure 12 shows that the maximum volume strain at peak gradually shifts from the middle zone of the surrounding rock to the top and bottom zones with the increase in height for the multi-scale surrounding rock with a width of 50 mm in the failure zone. The volume increasing zone is widely distributed in the surrounding rock with the increase in height. Figure 13 shows that the maximum volume strain at peak of the multi-scale surrounding rock with a height of 100 mm in failure zone gradually develops from the shallow surrounding rock to deep surrounding rock with the increase in width. Moreover, the volume strain of the shallow surrounding rock significantly increases.

Figure 14 illustrates the variation of the volume strain of the total, top, middle, and bottom zones with width and height at peak. In Fig. 14, the average volumetric strain (average value) is the ratio of the sum of the volumetric strains of different samples within a given scale interval to the number of samples. Figure 14a shows that the volume strain of the surrounding rock with a width of 50 mm in the failure zone decreases with the increase in height. The volume strain at a height of 20–140 mm is significantly greater than that at a height of 140–300 mm. The volume strain of the three zones is quite different when the height is 20–140 mm, and the volume strain in the middle zone is the largest. The volume strain of the three zones at a height of 140–300 mm is close, which is consistent with the cloud charts of the volume strain distribution in Fig. 12a–d. Figure 14b illustrates that the volume strain of the surrounding rock with a height of 100 mm in the failure zone stepped increases with the increase in width. The volume strain with a width of 20–70 mm is the smallest, and the average value of the total volume strain (total average value) is 0.0059; the volume strain with a width of 70–200 mm is in the middle, and the average value of total volume strain is 0.0141; the volume strain with a width of 200–300 mm is the largest, and the average value of total volume strain is 0.0184. The volume strain in the middle zone is still the largest, which is consistent with the cloud charts of the volume strain distribution in Fig. 13a–d.

Scale effect of the failure characteristics

Figures 15 and 16 show the failure characteristics of the surrounding rock to analyze the failure mechanism of the multi-scale surrounding rock. Only part scale diagrams are presented.

Figure 15 shows that the failure mode of the surrounding rock with a width of 50 mm in the failure zone gradually changes from shear failure to tensile shear failure with the increase in height. When the height is small, shear cracks are first formed at the top and bottom on the free surface side and gradually develop to middle and deep to form a V-shaped failure surface, as shown in Fig. 15a,b. When the height is large, shear cracks at the top and bottom develop to the middle and form a longitudinal tensile crack, as shown in Fig. 15c–d. The analysis shows that the failure mode is mainly shear failure and forms a V-shaped failure surface when the height to width ratio is small. The failure mode is mainly tensile shear failure and forms a longitudinal tensile surface when the height to width ratio is large, as shown in Fig. 15d.

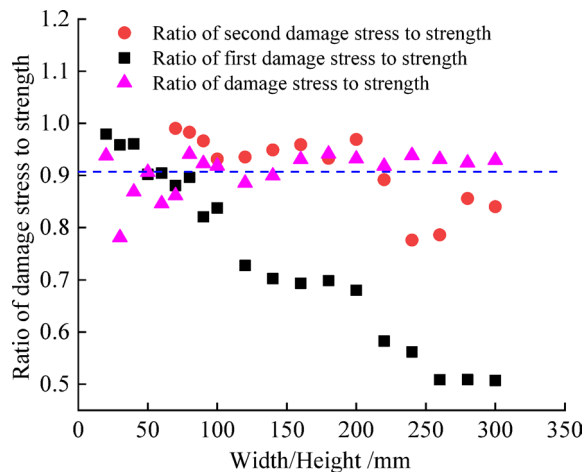


Fig. 11. Variation of the ratio of damage stress to strength.

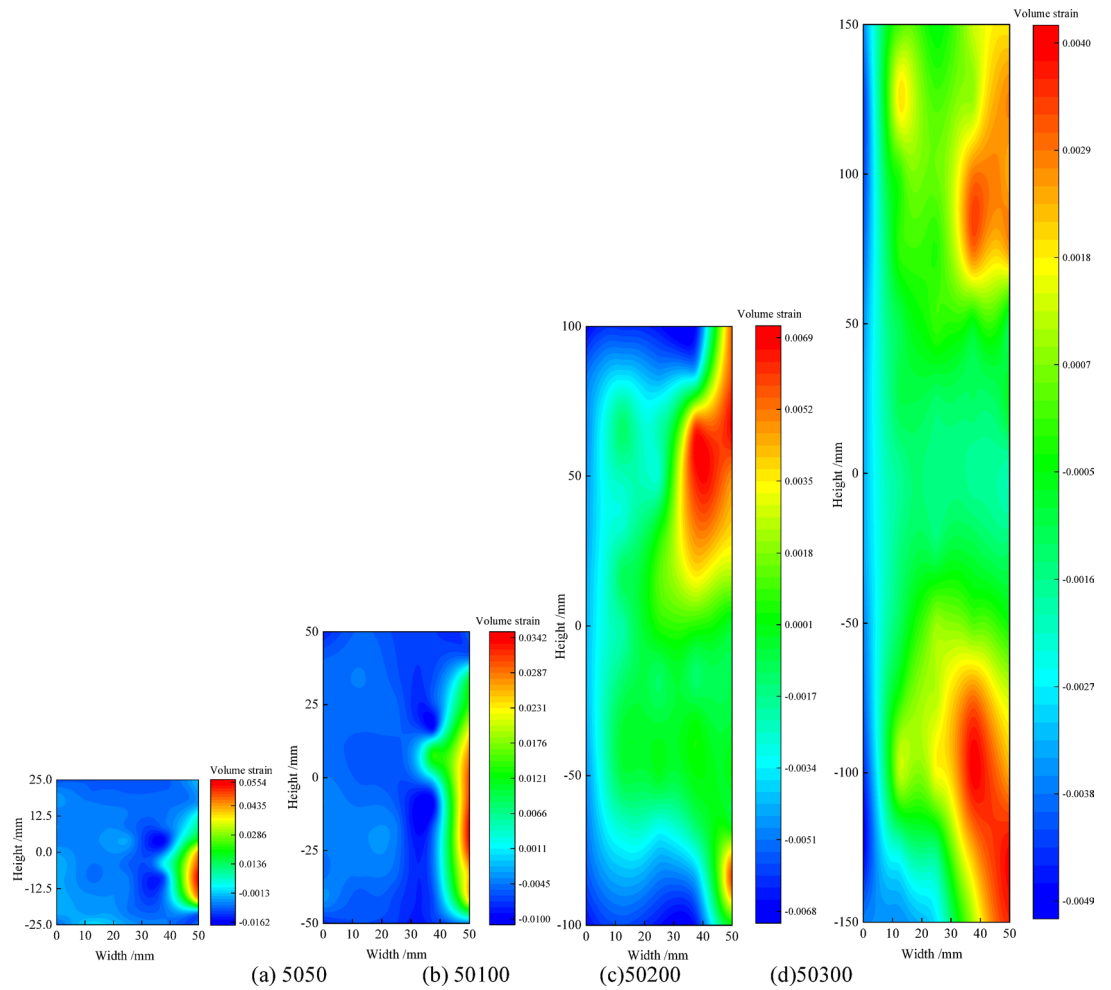


Fig. 12. Distribution characteristics of volume strain at peak (width 50 mm).

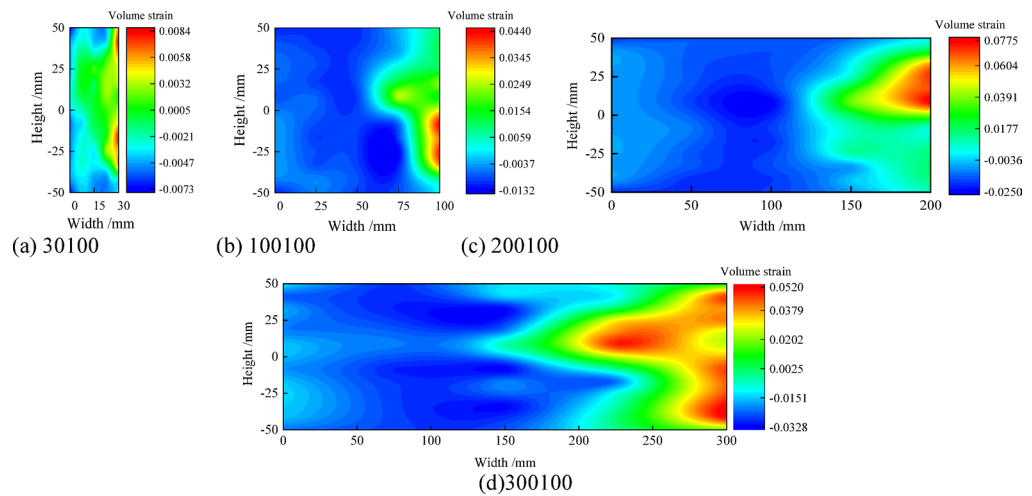


Fig. 13. Distribution characteristics of the volume strain at peak (height 100 mm).

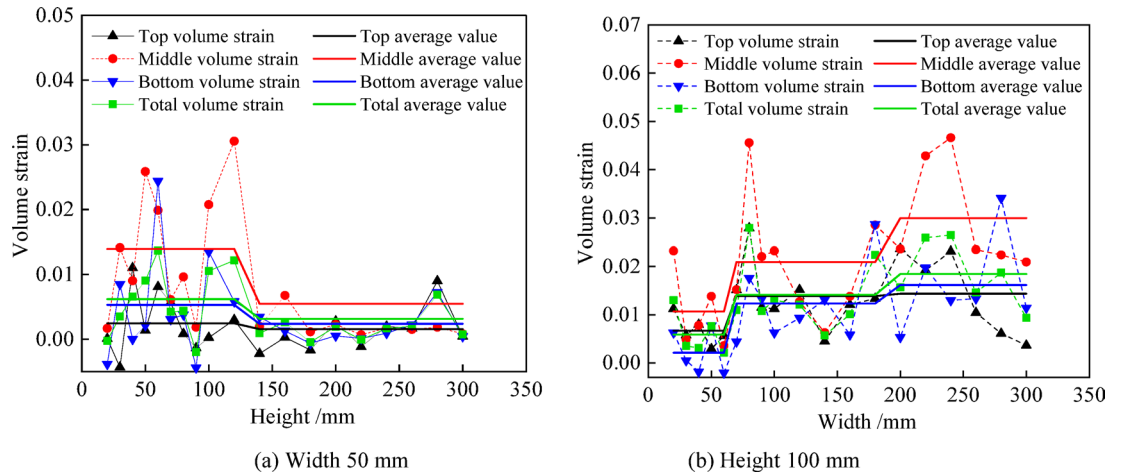


Fig. 14. Volume strain characteristics in different zones.

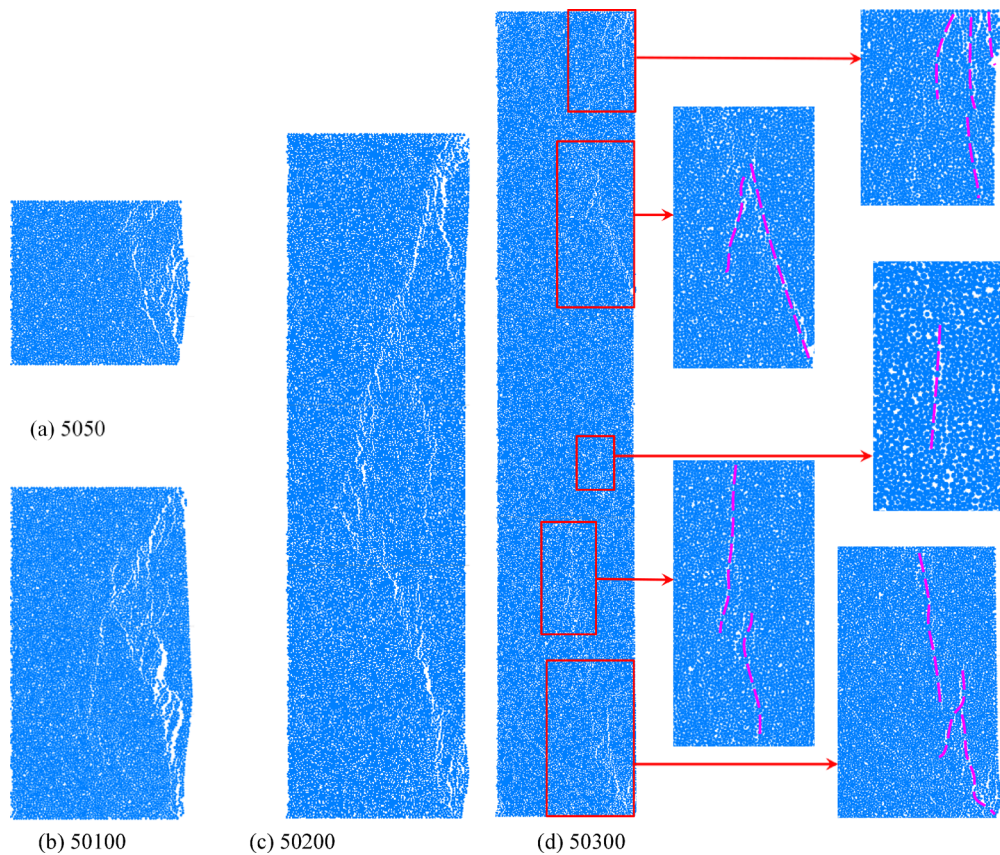


Fig. 15. Failure characteristics of the surrounding rocks at different heights (width 50 mm).

Figure 16 illustrates that the failure mode of the surrounding rock with a height of 100 mm in the failure zone changes from shallow to deep failure with the increase in width. The failure modes are shear failure, as shown in Fig. 16a–d. Shear failure occurs only in the shallow surrounding rock when the width is small. Shear failure simultaneously occurs in the shallow and deep surrounding rock when the width is large, which was called as the zonal disintegration found by researchers in roadway drilling.

According to the analysis of the multi-scale surrounding rock failure characteristics in Figs. 15 and 16, the rock mass is disturbed by excavation, which makes the stress readjust. When the stress concentration range formed in the surrounding rock of the roadway is narrow (in Fig. 17(a₃), the width of the stress concentration is W_1), the shear or tension shear failure occurs in the shallow surrounding rock, as shown in Figs. 15, 16a–b, and 17a₁–a₂, and the corresponding mechanical model is Fig. 17(a₃). When the stress concentration range formed

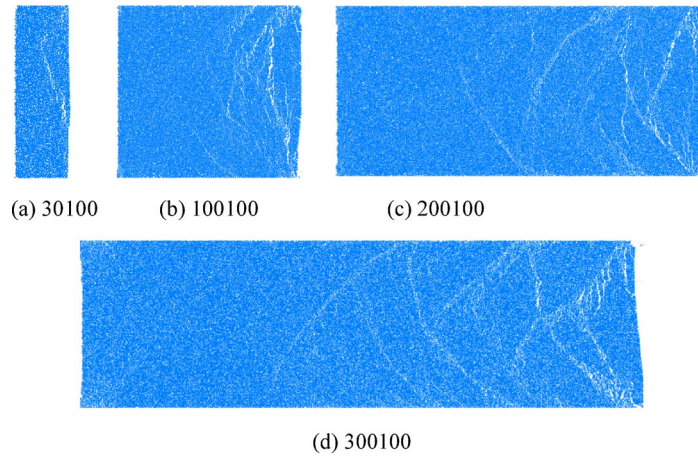


Fig. 16. Failure characteristics of the surrounding rocks at different widths (height 100 mm).

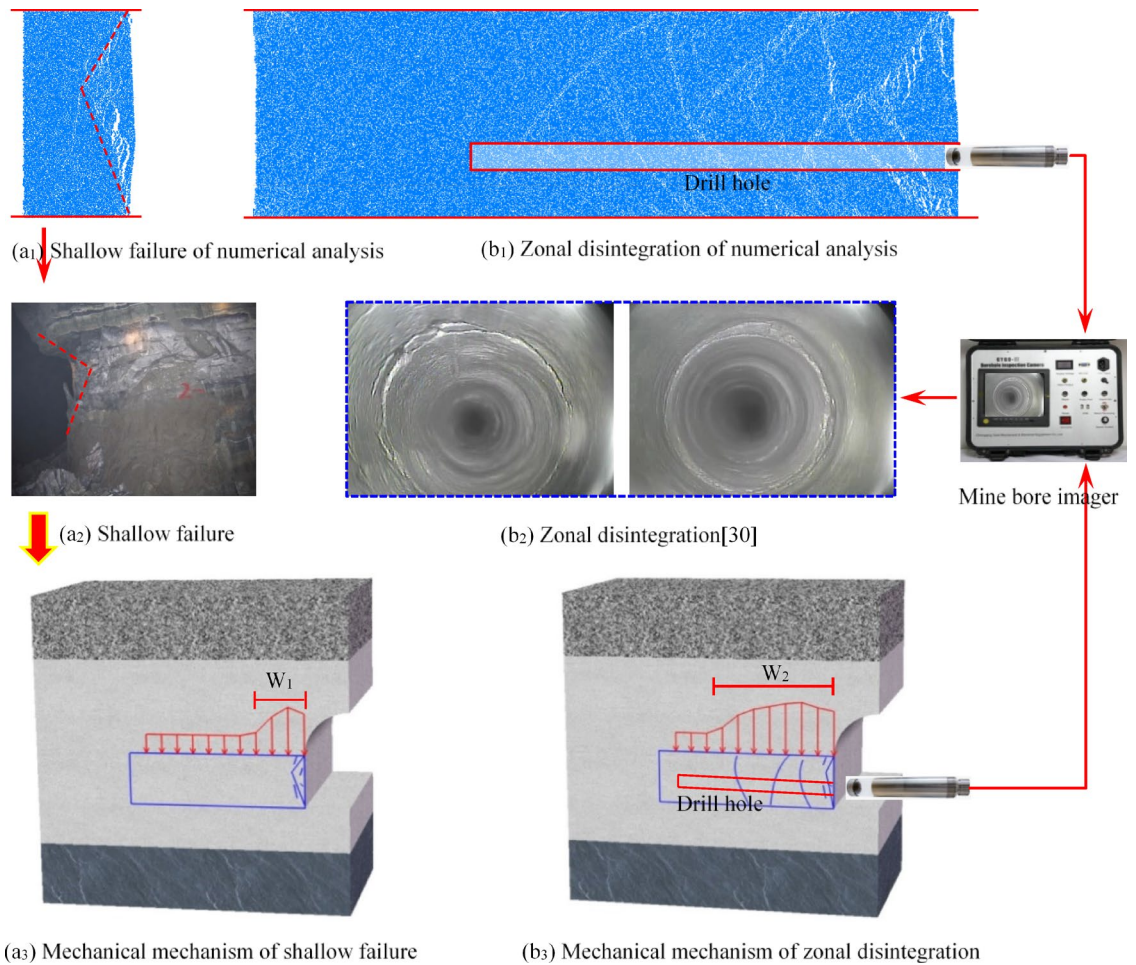


Fig. 17. Analysis of the mechanical mechanism of the surrounding rock failure.

in the surrounding rock of the roadway is wide (in Fig. 17(b₃), the width of the stress concentration is W_2), the shallow and deep surrounding rocks are damaged, which is the zonal disintegration found by researchers through roadway drilling, as shown in Figs. 16c–d and 17b₁–b₂ (Fig. 17b₂ cited in in reference [30]), and the corresponding mechanical model is Fig. 17(b₃).

The analysis of the multi-scale surrounding rock failure characteristics in Figs. 15, 16, and 17 reveals the mechanical mechanism of shallow failure and zonal disintegration failure of the surrounding rock. The

shallow failure of the surrounding rock occurs when the stress concentration range is narrow. Meanwhile, zonal disintegration failure of the surrounding rock occurs when the stress concentration range is wide. This mechanical mechanism perfectly explains the reason for the shallow and zonal disintegration failure of the surrounding rock. When the buried depth of the roadway is small, the in situ stress is small, the stress concentration range formed after excavation is narrow, and the failure mode of the surrounding rock is shallow failure under the action of the narrow stress concentration range (as shown in Fig. 17(a₃)). In deep mining mines, the roadway has a large buried depth and high in situ stress. The stress concentration formed after mining excavation is obvious, and the stress concentration range is wide. The failure mode of the surrounding rock under the action of wide stress concentration range is zonal disintegration (as shown in Fig. 17(b₃)).

Discussion

The surrounding rock analysis model is scientifically constructed by analyzing the failure characteristics of the roadway surrounding rock and compressively considering the damage and failure zones (Fig. 6). The free surface of the model simulates the free surface formed by roadway excavation. The failure zone simulates the failure by excavation, and the damage zone adjacent to the failure zone is the same type of rock that can be deformed together. Unlike the uniaxial test with free lateral surfaces or conventional triaxial test with confining pressure, this model more accurately reflects the actual stress state encountered in the underground engineering. From the failure characteristics of the multi-scale surrounding rock in Section "Scale effect of the failure characteristics", the failure forms of the surrounding rock at different scales are in good agreement with the failure characteristics of the surrounding rock observed in actual engineering, which once again proves the rationality of the construction of surrounding rock analysis model.

Conclusions

The strength, deformation, and failure mechanism of the multi-scale surrounding rock were studied through the surrounding rock analysis model. The following main conclusions were obtained.

- 1) The strength of the multi-scale surrounding rock with a width of 50 mm in the failure zone linearly decreases when the height is between 20 and 80 mm and linearly increases when the height is between 80 and 300 mm. Furthermore, the strength of the multi-scale surrounding rock with a height of 100 mm in the failure zone linearly increases when the width is between 20 and 300 mm.
- 2) The second damage stress appears in surrounding rock samples with a height of 100 mm and a width greater than 70 mm. The ratio of the second damage stress to the strength—as well as the ratio of the damage stress to the strength—approximately remains at 0.91.
- 3) Within the studied scale range, the peak volume strain decreases stepped for the multi-scale surrounding rock with a width of 50 mm as the height increases, the peak volume strain increases stepped for the multi-scale surrounding rock with the height of 100 mm as the width increases.
- 4) The mechanical mechanism of the shallow failure and zonal disintegration characteristics were revealed by analyzing the failure characteristics of multi-scale surrounding rock.

Data availability

All data generated or analysed during this study are included in this published article.

Received: 14 November 2025; Accepted: 31 December 2025

Published online: 19 January 2026

References

1. Yangsheng, Z. Retrospection on the development of rock mass mechanics and the summary of some unsolved centennial problems. *Chin. J. Rock Mech. Eng.* **40**(07), 1297–1336. <https://doi.org/10.13722/j.cnki.jrme.2021.0617> (2021).
2. Chuang, S., Yunhe, A., Jiaming, Z. & Shuai, W. Particle flow of meso-fracture characteristics and macro-scale effect of granites. *Chin. J. Geotech. Eng.* **42**(09), 1687–1695. <https://doi.org/10.11779/CJGE202009013> (2020).
3. Darlington, W. J., Ranjith, P. G. & Choi, S. K. The effect of specimen size on strength and other properties in laboratory testing of rock and rock-Like cementitious brittle materials. *Rock Mech. Rock Eng.* **44**, 513–529. <https://doi.org/10.1007/s00603-011-0161-6> (2011).
4. Zaytsev, D. V., Kochanov, A. N., Panteleev, I. A. & Panfilov, P. Y. Influence of the scale effect in testing the strength of rock samples. *Bull. Russ. Acad. Sci. Phys.* **81**, 337–340. <https://doi.org/10.3103/S1062873817030406> (2017).
5. Asadi, P., Ashrafi, M. J. & Fakhimi, A. Physical and numerical evaluation of effect of specimen size on dynamic tensile strength of rock. *Comput. Geotech.* **142**, 104538. <https://doi.org/10.1016/j.compgeo.2021.104538> (2022).
6. Kaihui, Li., Yungming, C., Zhenyu, Y., Dongya, H. & Jingjing, M. Size effects in a transversely isotropic rock under Brazilian tests: Laboratory testing. *Rock Mech. Rock Eng.* **53**, 2623–2642. <https://doi.org/10.1007/s00603-020-02058-7> (2020).
7. Weisheng, L., Qian Guian, Yu. & Zhishui, B. F. Statistical size scaling of compressive strength of quasi-brittle materials incorporating specimen length-to-diameter ratio effect. *Theoret. Appl. Fract. Mech.* **104**, 102345. <https://doi.org/10.1016/j.tafmec.2019.102345> (2019).
8. Kashfi, M., Shad, S. & Zivar, D. Evaluation of sample scale effect on geomechanical tests. *Petrol. Res.* <https://doi.org/10.1016/j.ptlrs.2022> (2022).
9. Jun, C., Renshu, Y. & Yiqiang, K. Influence of the Rock length-to-diameter ratio and failure modes on uniaxial compression strength. *Geotech. Geol. Eng.* **38**, 2551–2557. <https://doi.org/10.1007/s10706-019-01168-6> (2020).
10. Ruipeng, Q. et al. Effect of water intrusion on mechanical behaviors and failure characteristics of backfill body and coal pillar composite specimens under uniaxial compression. *J. Clean. Prod.* **502**, 145388. <https://doi.org/10.1016/j.jclepro.2025.145388> (2025).
11. Xioze, W. et al. Strength deterioration mechanism of sandstone subjected to low-frequency dynamic disturbance under the varying static pre-stress levels. *Rock Mech. Rock Eng.* <https://doi.org/10.1007/s00603-025-04914-w> (2025).

12. Javad, A. M., Abdolhadi, G. & Amirasad, F. S. A new peak shear strength criterion of three-dimensional rock joints considering the scale effects. *Arab. J. Geosci.* **14**, 936. <https://doi.org/10.1007/s12517-021-07319-5> (2021).
13. Tao, D. et al. Size effect on mechanical properties of rock-like materials with three joints. *Geotech. Geol. Eng.* **38**, 4073–4089. <https://doi.org/10.1007/s10706-020-01279-5> (2020).
14. Chong, Ma., Wenmin, Y., Yuan, Y. & Li, J. Simulating strength parameters and size effect of stochastic jointed rock mass using DEM Method. *KSCE J. Civ. Eng.* **22**, 4872–4881. <https://doi.org/10.1007/s12205-017-1581-y> (2018).
15. Shuguang, Z., Chen Lei, Lu. & Pingping, L. W. Discussion on failure mechanism and strength criterion of sandstone based on particle discrete element method. *KSCE J. Civ. Eng.* **25**, 2314–2333. <https://doi.org/10.1007/s12205-021-2031-4> (2021).
16. Peitao, W., Yang Tianhong, Xu., Tao, C. M. & Changhong, Li. Numerical analysis on scale effect of elasticity, strength and failure patterns of jointed rock masses. *Geosci. J.* **20**(4), 539–549. <https://doi.org/10.1007/s12303-015-0070-x> (2016).
17. Bewick, R. P. The Strength of massive to moderately jointed rock and its application to cave mining. *Rock Mech. Rock Eng.* **54**, 3629–3661. <https://doi.org/10.1007/s00603-021-02466-3> (2021).
18. Wanrong, L., Jiankang, L. & Chun, Z. Multi-scale effect of acoustic emission characteristics of 3D rock damage. *Arab. J. Geosci.* **12**, 668. <https://doi.org/10.1007/s12517-019-4864-4> (2019).
19. Mei, Li., Hong, H., Yanchao, S. & Yifei, H. Specimen shape and size effects on the concrete compressive strength under static and dynamic tests. *Constr. Build. Mater.* **161**, 84–93. <https://doi.org/10.1016/j.conbuildmat.2017.11.069> (2018).
20. Brook, N. The equivalent core diameter method of size and shape correction in point load testing. *Int. J. Rock Mech. Min. Sci. Geomech. Abstracts* **22**(2), 61–70. [https://doi.org/10.1016/0148-9062\(85\)92328-9](https://doi.org/10.1016/0148-9062(85)92328-9) (1985).
21. Rajmeny, P. K., Singh, U. K. & Rathore, S. S. A new model to estimate rock mass strength accounting for the scale effect. *Int. J. Rock Mech. Min. Sci.* **41**(4), 1013–1021. <https://doi.org/10.1016/j.ijrmms.2004.03.008> (2004).
22. Ivan, P. The strength criterion for rocks under true triaxial stress. *Proc. Struct. Integr.* **32**, 166–172. <https://doi.org/10.1016/j.prostr.2021.09.024> (2021).
23. Masoumi, H., Saydam, S. & Hagan, P. C. Incorporating scale effect into a multiaxial failure criterion for intact rock. *Int. J. Rock Mech. Min. Sci.* **83**, 49–56. <https://doi.org/10.1016/j.ijrmms.2015.12.013> (2016).
24. Mehranpour, M. H., Kulatilake, P. H., Xingen, M. & He, M. Development of new three-dimensional rock mass strength criteria[J]. *Rock Mech. Rock Eng.* **51**, 3537–3561. <https://doi.org/10.1007/s00603-018-1538-6> (2018).
25. Arsalan, M. et al. Machine learning techniques to predict rock strength parameters. *Rock Mech. Rock Eng.* <https://doi.org/10.1007/s00603-021-02747-x> (2022).
26. Lisjak, A. & Grasselli, G. A review of discrete modeling techniques for fracturing processes in discontinuous rock masses. *J. Rock Mech. Geotech. Eng.* **6**, 301–314. <https://doi.org/10.1016/j.jrmge.2013.12.007> (2014).
27. Cundall, P. A. & Strack, O. A discrete numerical model for granular assemblies. *Géotechnique* **30**(3), 331–336 (2008).
28. Potyondy, D. O. & Cundall, P. A. A bonded-particle model for rock. *Int. J. Rock Mech. Min. Sci.* **41**(8), 1329–1364. <https://doi.org/10.1016/j.ijrmms.2004.09.011> (2004).
29. Wang, Y., Su, H., Wang, L., Jiao, H. & Li, Z. Study on the difference of deformation and strength characteristics of three kinds of sandstone. *J. China Coal Soc.* **45**(04), 1367–1374. <https://doi.org/10.13225/j.cnki.jccs.2019.0418> (2020).
30. Shuca, Li. et al. In-situ monitoring research on zonal disintegration of surrounding rock mass in deep mine roadway. *Chin. J. Rock Mech. Eng.* **27**(8), 1545–1553 (2008).

Author contributions

Wu and Wang wrote the main manuscript text; Xie assisted in experiments and validated the data. All authors reviewed the manuscript.

Funding

This work was financially supported by the Youth Science Fund Project of the National Natural Science Foundation of China (51804129); Jiangsu Postdoctoral Research Funding Program (2019K139); and Suzhou City University National-Level Pre-research Project (2024SGY017).

Declarations

Competing interests

The authors declare that they have no known competing financial interests or personal relationships that could have appeared to influence the work reported in this paper.

Additional information

Correspondence and requests for materials should be addressed to F.X.

Reprints and permissions information is available at www.nature.com/reprints.

Publisher's note Springer Nature remains neutral with regard to jurisdictional claims in published maps and institutional affiliations.

Open Access This article is licensed under a Creative Commons Attribution-NonCommercial-NoDerivatives 4.0 International License, which permits any non-commercial use, sharing, distribution and reproduction in any medium or format, as long as you give appropriate credit to the original author(s) and the source, provide a link to the Creative Commons licence, and indicate if you modified the licensed material. You do not have permission under this licence to share adapted material derived from this article or parts of it. The images or other third party material in this article are included in the article's Creative Commons licence, unless indicated otherwise in a credit line to the material. If material is not included in the article's Creative Commons licence and your intended use is not permitted by statutory regulation or exceeds the permitted use, you will need to obtain permission directly from the copyright holder. To view a copy of this licence, visit <http://creativecommons.org/licenses/by-nc-nd/4.0/>.

© The Author(s) 2026